

Final Accepted Paper

Ref.: VISI348-00

Editor: Prof. J. Malik

Date of submission: 6 February 2003

Title: Robust Photometric Invariant Region Detection in Multispectral Images

Corresponding author:

Theo Gevers

Intelligent Sensory Information Systems, Faculty of Science,

University of Amsterdam, Kruislaan 403,

1098 SJ Amsterdam, The Netherlands.

Index terms

Photometric invariance, region detection, clustering, multispectral images, noise robustness, camera calibration, polar angle representation.

Listing of Footnotes

Correspondence: Theo Gevers, Intelligent Sensory Information Systems, Faculty of Science, University of Amsterdam, Kruislaan 403, 1098 SJ Amsterdam, The Netherlands.

Robust Photometric Invariant Region Detection in Multispectral Images

Th. Gevers and H. M. G. Stokman

Abstract

Our aim is to detect photometric invariant regions in multispectral images robust against sensor noise. Therefore, different polar angle representations of a spectrum are examined for invariance using the dichromatic reflection model. These invariant representations take advantage of white balancing. Based on the camera sensitivity, a theoretical expression is obtained of the certainty associated with the polar angular representations under the influence of noise. The expression is employed by the segmentation technique to ensure robustness against sensor noise.

1 Introduction

Multispectral imaging has received a great deal of attention recently. Spectral imaging is used, for example, in remote sensing, computer vision, and industrial applications. Spectral information has become an important quality factor in many industrial processes because of its high accuracy [12]. Spectral images can be obtained, for example, by a CCD-camera with narrow-band interference filters [14]. Tominaga [24] [25] describes two generations of a multichannel vision system based on the use of a CCD-camera and six color filters to reconstruct the surface spectral reflectance and illuminant spectral power distribution. Baronti

et al. [3] uses a multispectral imaging system for the non-invasive analysis of works of art. Haneishi *et al.* [11] uses five color filters for archiving spectral images of art works.

In the past, various color image segmentation methods have been proposed which do not account for the image formation process [6] [18]. A drawback of these color segmentation methods is that the values of the color features, on which the segmentation method relies, depend on the geometry of the object, the viewpoint of the camera and on the illumination conditions. As a consequence, the obtained segmentation results may be affected negatively by shadows, shading and highlights. In contrast, image processing methods that account for the process of image formation have been studied since the mid-1980s, see for instance the work collected by Wolff, Shafer and Healey [26]. Shafer [22] presented the dichromatic reflection model, a physical model of reflection which states that two distinct types of reflection - surface and body reflection - occur, and that each type can be decomposed into a relative spectral distribution and a geometric scale factor. Klinker *et al.* [16] developed a color segmentation algorithm based on the Shafer's model. The method is based on evaluating characteristic shapes of clusters in red-green-blue (*RGB*) space followed by segmentation independent of the object's geometry, illumination and highlights. To achieve robust image segmentation, however, surface patches of objects in view must have a rather broad distribution of surface normals which may not hold for objects in general. Bajcsy [2] developed a similar image segmentation method using the *H-S* color space instead of the *RGB*-color space. Healey [13] proposed a method to segment images on the basis of normalized color. However, Kender [15] showed that normalized color and hue are singular at some *RGB* values and unstable at many others. For instance, the essential singularity of normalized coordinates is at black ($R = G = B = 0$), whereas for the hue the singularity is at the achromatic axis ($R = G = B$). As a consequence, both color spaces become unstable near the singularity where a small perturbation of *RGB* value might cause a large jump in the transformed values. Traditionally, these effects are either ignored or suppressed by an ad hoc thresholding of the

transformed values. For example, Ohta [20] rejects normalized color values if the sum of RGB is less than 30, and rejects hue values if the saturation times the intensity is less than 9. Healey [13] rejects all sensor measurements that fall within the sphere of radius 4σ centered at the origin in RGB -space.

A more elegant strategy to deal with unstable color values would be to generate the reliability of a transformed color together with the output and to incorporate the reliability in the image processing method. An early effort in this direction is the work of Burns and Berns [5]. The authors analyze the error propagation from a measured color signal transformed into the CIE $L^*a^*b^*$ color space. In this way, an indication is obtained of how the color space transform influences the mean, variance and covariance of the colors under the influence of noise. Shafarenko, Petrou and Kittler [21] use an adaptive filter for noise reduction in the CIE $L^*u^*v^*$ space prior to 3-D color histogram construction. The filter width depends on the covariance matrix of the noise distribution in the CIE $L^*u^*v^*$ space.

Obviously, photometric invariance is essential for image segmentation. However, another major requirement is robustness against noise which is amplified by the instabilities of the photometric invariant transformations. Our aim is to propose techniques to detect regions in multispectral images which are invariant to photometric variations and which are, at the same time, robust to substantial noise. Therefore, the contribution of this paper is two-fold:

1. Photometric Invariance: We propose two polar coordinate models to encode spectra and analyze these models for invariance to photometric effects using the dichromatic reflection model for the purpose of image segmentation.
2. Noise Robustness: We propose computational models for estimating the effect of sensor noise on the stability of the polar coordinates. The expression of the reliability of the polar coordinate representation is incorporated in the segmentation method.

As the segmentation method is based on the physics-based dichromatic reflec-

tion model, it is possible to characterize what kinds of images are likely to be segmented successfully by our algorithm. The model describes the reflection of materials which are optically inhomogeneous. In that case the light interacts with a medium that causes the bigger component of surface matter, as well as with particles of a colorant to produce scattering and coloration. Many common materials have these characteristics, including most paints, varnishes, paper, ceramics, and plastics. Therefore, we anticipate that images of objects of these materials are properly segmented by the proposed method. As a consequence, the proposed method is unsuited for homogeneous materials. Further, it is assumed that the light source is spectrally uniform over the scene.

The paper is organized as follows. In section 2, the dichromatic reflection reflection model and a camera model are described in detail. In section 3, distance measures are proposed and examined for photometric invariance. In section 4, the effect of sensor noise is propagated through the polar angle representations of spectra. The photometric invariant region detection methods are described in section 5. In section 6, the theoretical estimated uncertainty in polar angular representation is compared empirically to the real uncertainty. Experiments are carried out to evaluate the invariance to photometric effects of the proposed segmentation methods. A discussion is given in section 7.

2 Reflection and Camera Models

In this section, we discuss a camera and image formation model. Based on the models, we examine cluster shapes drawn by uniformly colored objects in multispectral color space.

2.1 Multispectral Imaging

In this paper, we use the Inspector V7 spectrograph from spectral Imaging Ltd. The spectrograph transforms the monochrome CCD-camera to a line scanner: One axis displays the spatial information, whereas along the other axis the vis-

ible wavelength range is recorded generating an image $h(x, \lambda)$ for each position (x, λ) . In this paper, the Jain CV-M300 camera is used with 576 pixels along the optical axis. We use the Inspector V7 spectrograph with shortest observable wavelength of 410 nm and longest wavelength of 700 nm. The wavelength interval corresponds to 5 nm.

2.2 Camera and Image Formation Models

We use a linear camera model to describe the relation between input signal h_i and the output signal c_i for the i th color channel at position \vec{x} as

$$c_i(\vec{x}, \lambda) = \gamma_i h_i(\vec{x}, \lambda) + d(\vec{x}) \quad (1)$$

where $d(\vec{x})$ denotes the dark current independent of the wavelength and γ_i denotes the camera gain for the i th color channel. For the moment, we ignore the dark current for notational simplicity. For the same reason, the notation for the position is left out.

The camera gain may further be refined as consisting of two terms

$$\gamma_i = \gamma_e \cdot \gamma_{w,i} \quad (2)$$

where γ_e denotes the electronic gain and $\gamma_{w,i}$ denotes the white-balancing gain.

For inhomogeneous, dielectric materials, the measured input signal h_i of (1) is described by the dichromatic reflection model [22]. To be precise, let $E(\vec{x}, \lambda)$ be the spectral power distribution of the incident (ambient) light at the object surface at \vec{x} , and let $L(\vec{x}, \lambda)$ be a function based on the geometric and spectral properties of the object surface at \vec{x} . The spectral sensitivity of the i th sensor is given by $f_i(\lambda)$. Then g_i , the camera output of the i th channel (no camera gain) is given by:

$$g_i(\vec{x}, \lambda) = \int_{\lambda} E(\vec{x}, \lambda) L(\vec{x}, \lambda) f_i(\lambda) d\lambda \quad (3)$$

where λ denotes the wavelength. The integral is taken from the visible spectrum (e.g. 410-700 nm). In the remainder, we will leave out the notation of position \vec{x} .

Then, for an opaque inhomogeneous dielectric object, the geometric and surface reflection component of function $L(\vec{x}, \lambda)$ can be decomposed in a body and surface reflection component as described by Shafer [22]:

$$h_i(\lambda) = m_b(\vec{n}, \vec{s}) \int_{\lambda} f_i(\lambda) E(\lambda) c_b(\lambda) d\lambda + m_s(\vec{n}, \vec{s}, \vec{v}) \int_{\lambda} f_i(\lambda) E(\lambda) c_s(\lambda) d\lambda \quad (4)$$

denoting the camera output (without the camera gain) for filter f_i with central wavelength i . Further, $c_b(\lambda)$ and $c_s(\lambda)$ are the surface albedo and Fresnel reflectance respectively, \vec{n} is the surface patch normal, \vec{s} is the direction of the illumination source, and \vec{v} is the direction of the viewer. Geometric terms m_b and m_s denote the geometric dependencies on \vec{n}, \vec{s} and \vec{v} . In this paper, we make no specific assumptions for functions m_b and m_s but simply require that

$$0 \leq m_b(\vec{n}, \vec{s}), m_s(\vec{n}, \vec{s}, \vec{v}) \leq 1 \quad (5)$$

It is important to observe that (5) captures one of the attractive features of the dichromatic reflection model: the model is far more general than typical models used in computer vision and computer graphics, and includes most such models as special cases. For instance, a possible instantiation of m_b is Lambert's cosine law (then $m_s = 0$). Similarly, a possible instantiation of both m_b and m_s is Phong's model for specular reflection [4].

2.3 White-Balancing

According to (4), a matte, white reference standard with constant spectral response can be described by $c_b(\lambda) = 1$ and $m_b(\vec{n}, \vec{s}) = 1$. Furthermore, assume that the camera is not white-balanced so $\gamma_{w,i} = 1$, say, for all color channels i . The measured sensor values are obtained substituting the body reflection of (4) in (1) as

$$w_i(\lambda) = \gamma_e \int_{\lambda} f_i(\lambda) E(\lambda) d\lambda \quad (6)$$

denoting the sensor response for the white matte reference standard. The gain parameter $\gamma_{w,i}$ of (2) is adjusted, either by the white-balancing procedure of the

CCD-camera or else manually, as

$$\gamma_{w,i} = \frac{1}{w_i(\lambda)} \quad (7)$$

Then the output of a white-balanced camera system is as follows

$$c_i(\lambda) = \frac{\gamma_e m_b(\vec{n}, \vec{s}) \int_{\lambda} f_i(\lambda) E(\lambda) c_b(\lambda) d\lambda}{\gamma_e \int_{\lambda} f_i(\lambda) E(\lambda) d\lambda} + \frac{\gamma_e m_s(\vec{n}, \vec{s}, \vec{v}) \int_{\lambda} f_i(\lambda) E(\lambda) c_s(\lambda) d\lambda}{\gamma_e \int_{\lambda} f_i(\lambda) E(\lambda) d\lambda} \quad (8)$$

Considering the neutral interface reflection (NIR) model [22] (assuming that $c_s(\lambda)$ has a nearly constant value independent of the wavelength), we obtain $c_s(\lambda) = c_s$. Then the specular term of (8) rewrites to

$$s_i(\lambda) = \frac{m_s(\vec{n}, \vec{s}, \vec{v}) c_s \int_{\lambda} f_i(\lambda) E(\lambda) d\lambda}{\int_{\lambda} f_i(\lambda) E(\lambda) d\lambda} = m_s(\vec{n}, \vec{s}, \vec{v}) c_s \quad (9)$$

making the surface reflection term of (4) independent of the spectral distribution of the light source. Due to the white-balancing operation and the neutral interface reflection assumption, the color channels $c_i(\lambda)$ produce equal output when an achromatic object is imaged.

Further, in case of the Inspector V7 spectrograph, we have narrow band filters $f(\lambda_i)$, which can be modeled as a unit impulse that is shifted over i wavelengths: The transmission at $\lambda_i = \delta$ and zero elsewhere. Note the subtle difference between $f_i(\lambda)$ and $f(\lambda_i)$. $f_i(\lambda)$ denotes a broad-band color filter (integrating over various wavelengths) with central wavelength i . $f(\lambda_i)$ denotes a narrow-band filter of unit impulse at wavelength i . Then (9) rewrites to

$$s(\lambda_i) = \frac{m_s(\vec{n}, \vec{s}, \vec{v}) E(\lambda_i) c_s}{E(\lambda_i)} = m_s(\vec{n}, \vec{s}, \vec{v}) c_s \quad (10)$$

again independent of λ and consequently invariant to the spectral distribution of the light source. Further, assuming narrow-band filters, (8) rewrites to

$$c(\lambda_i) = \frac{m_b(\vec{n}, \vec{s}) E(\lambda_i) c_b(\lambda_i)}{E(\lambda_i)} + \frac{m_s(\vec{n}, \vec{s}, \vec{v}) E(\lambda_i) c_s}{E(\lambda_i)} = m_b(\vec{n}, \vec{s}) c_b(\lambda_i) + m_s(\vec{n}, \vec{s}, \vec{v}) c_s \quad (11)$$

corresponding to the camera output at wavelength λ_i making the whole dichromatic reflection model of (4) independent of the spectral distribution of the light

source (i.e. color constancy). In vector notation, a spectrum is denoted as

$$\vec{c} = m_b(\vec{n}, \vec{s})\vec{c}_b + m_s(\vec{n}, \vec{s}, \vec{v})\vec{c}_s \quad (12)$$

The vectors $\vec{n}, \vec{s}, \vec{v}$ are three-dimensional. The vectors $\vec{c}, \vec{c}_b, \vec{c}_s$ are N -dimensional, with N the number of samples taken in the wavelength range. Although standard video camera's are not equipped with narrow-band filters, spectral sharpening can be used to achieve this to a large extent [8].

2.4 Cluster Shapes in Sensor Space

Consider the camera output for a white-balanced camera described in (12). According to the body reflection term, the color depends on \vec{c}_b and the brightness on $m_b(\vec{n}, \vec{s})$. If a matte surface region (i.e. the specular term is zero), which is homogeneously colored (i.e. with constant albedo), contains a variety of surface normals, then the set of measured colors will generate an elongated color cluster in sensor space, where the direction of the streak is determined by \vec{c}_b and its extent by the variations of surface normals \vec{n} with respect to the illumination direction \vec{s} . As a consequence, a uniformly colored surface which is curved (i.e. varying surface orientation) gives rise to a broad variance of brightness (i.e. $m_b(\vec{n}, \vec{s})$) but not in color (i.e. the same \vec{c}_b). Since no negative sensor values occur, a precise formulation of \vec{c}_b is the notion of a vector in the positive quadrant of in vector space. Hence, for a unit 3-D color cube, \vec{c}_b is constrained to be less than or equal to unity in each dimension, see Figure 1.

For a shiny surface, the observed highlight is defined by vector \vec{c}_s (with equal values), which is on the main diagonal of the unit color cube corresponding to the grey-values. Further, the extent of \vec{c}_s is affected by the surface geometry and viewing direction. Then, according to (12), the observed colors of a shiny surface (i.e. uniformly colored and containing highlights) must be on a plane. The plane is spanned by vectors \vec{c}_b and \vec{c}_s , where \vec{c}_s defines the main diagonal, see Figure 1.

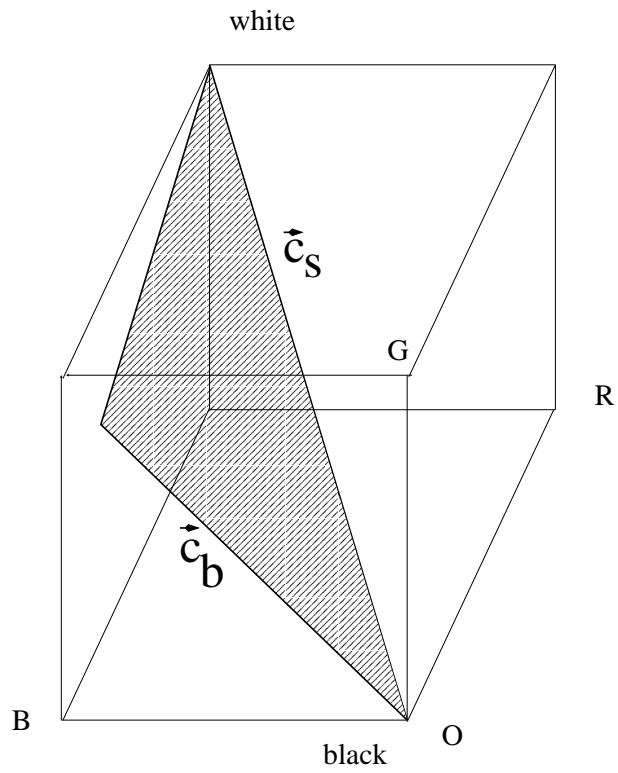


Figure 1: *The unit-constrained vector (unit half-ray) \vec{c}_b is drawn by a matte surface in RGB-space. Similarly, the plane defined by \vec{c}_b and \vec{c}_s is drawn by a shiny surface in RGB.*

3 Photometric Invariant Distance Measures

Uniformly colored matte objects draw unit-constrained vectors (half-rays) in multispectral color space due to changes in the surface orientation, illumination intensity and shading. In addition, due to specularities, shiny objects draw half-planes in multispectral space. For photometric invariant region detection, we aim to model the shape of the clusters as either a half-ray or a half-plane. A measured spectrum is then assigned to one of these clusters based on the minimal distance of the spectrum to the clusters. Various distance measures have been proposed. For example, Androutsos *et al.* [1] proposed a combination distance measure which is composed of an angle and magnitude component. However, the distance measure is not a photometric invariant. On the other hand, the distance from a spectrum to a line is a photometric invariant for matte objects. Similarly, the distance from a spectrum to a plane is a photometric invariant for shiny objects [9, 10]. However, the drawback of the computation of the distance from a spectrum to a plane is that opponent colors map onto the same plane. Therefore, the angular representation of spectra is proposed in this section.

3.1 Distance between Chromaticity Polar Angles

Spectra can be transformed into polar coordinates. To define polar coordinates descriptors, the origin O and a positive horizontal axis are fixed. Then each N -dimensional point \vec{P} can be located by assigning to it polar coordinates $(\rho, \vec{\theta})$ where the one-dimensional term ρ gives the distance from O to \vec{P} and the $(N - 1)$ -dimensional term $\vec{\theta}$ gives the angles from the initial axis to \vec{P} .

A spectrum defined by (11) is transformed to its polar coordinate representation as

$$\rho_t = |\vec{c}| \quad (13)$$

$$\theta_c(\lambda_i) = \arctan\left(\frac{c(\lambda_i)}{c(\lambda_N)}\right), \quad 1 \leq i \leq N - 1 \quad (14)$$

where ρ_t encodes the intensity of the spectrum and $\theta_c(\lambda_i)$ the chromaticity of the spectrum. $\theta_c(\lambda_i)$ takes on values in the range $0 \leq \theta_c \leq \frac{\pi}{2}$.

For the analysis of photometric invariance of the chromaticity angular representation of spectra, substitution of the body reflection term of (11) in (14) gives

$$\theta_c(\lambda_i) = \arctan \left(\frac{m_b(\vec{n}, \vec{s})c_b(\lambda_i)}{m_b(\vec{n}, \vec{s})c_b(\lambda_N)} \right) = \arctan \left(\frac{c_b(\lambda_i)}{c_b(\lambda_N)} \right) \quad (15)$$

independent of geometry term $m_b(\vec{n}, \vec{s})$.

The quadratic distance, e , between any two M -dimensional vectors of angles $\vec{\theta}_1$ and $\vec{\theta}_2$ is defined as follows:

$$e^2(\vec{\theta}_1, \vec{\theta}_2) = \sum_{i=1}^M (\Delta(\theta_{1i}, \theta_{2i}))^2, \quad 0 \leq \theta_{1i}, \theta_{2i} < 2\pi \quad (16)$$

Here, θ_{1i} denotes the i th of M angles for the first vector. The distance $\Delta(\theta_i, \theta_j)$ takes values in the interval $[0, 2]$ and is defined as follows:

$$\Delta(\theta_i, \theta_j) = [(\cos(\theta_i) - \cos(\theta_j))^2 + (\sin(\theta_i) - \sin(\theta_j))^2]^{1/2} \quad (17)$$

The angular difference Δ is indeed a distance because it satisfies the following metric criteria:

- $\Delta(\theta_i, \theta_j) \geq 0$ for all θ_i and θ_j
- $\Delta(\theta_i, \theta_j) = 0$ if and only if $\theta_i = \theta_j$
- $\Delta(\theta_i, \theta_j) = \Delta(\theta_j, \theta_i)$ for all θ_i and θ_j
- $\Delta(\theta_i, \theta_j) + \Delta(\theta_j, \theta_k) \geq \Delta(\theta_i, \theta_k)$ for all θ_i, θ_j , and θ_k

The proof of the first three conditions is trivial. To see the triangular inequality, consider two angles θ_i, θ_j . Define

$$\vec{\theta}_i = [\cos(\theta_i) \quad \sin(\theta_i)]^T \quad (18)$$

and define $\vec{\theta}_j$ in similar fashion. Since $\Delta(\theta_i, \theta_j) = d(\vec{\theta}_i, \vec{\theta}_j)$ where d denotes the well-known Euclidean distance, the triangular inequality is proven.

Since chromaticity polar angles are independent of the geometry of the object, as was shown in (15), the distance between two chromaticity angles is photometric invariant as well.

3.2 Distance between Hue Polar Angles

Consider a N -dimensional spectrum \vec{c} defined by (11) transformed to a different polar coordinate representation as follows

$$\rho_s = 1 - \min\{c(\lambda_1), \dots, c(\lambda_N)\} \quad (19)$$

$$\theta_h = \alpha[c(\lambda_i) - [1 - \rho_s], \phi(i, N)] \quad (20)$$

where θ_h takes on values in the range $0 \leq \theta_h < 2\pi$ and where

$$\phi(i, N) = \frac{i-1}{N-1} \cdot \frac{4}{3}\pi \quad (21)$$

and

$$\alpha(w_i, \theta_i) = \arctan \left(\frac{\sum_{i=1}^N w_i \sin(\theta_i)}{\sum_{i=1}^N w_i \cos(\theta_i)} \right), \quad (22)$$

The function ϕ takes on values in the range $0 \leq \phi(i, N) \leq \frac{4}{3}\pi$. The function α takes on values in the range $0 \leq \alpha < 2\pi$. The function denotes the weighted average of a series of N angles θ_i with corresponding weight w_i . The average is computed by decomposing the angular value into a horizontal and vertical component. The saturation of the spectrum is encoded by ρ_s . The angle θ_h can be thought of as the hue obtained directly from multispectral data. The function $\phi(i, N)$ assigns a hue-angle to the i th of N spectral samples. The range from $0 \dots 4/3\pi$ is reserved for the colors ranging from red through green through blue, so that the range from $4/3\pi \dots 2\pi$ represents the purplish colors. The choice of $4/3\pi$ is somewhat arbitrary but can be defended by taking the hue computation into account based on conventional red-green-blue colors where a similar division is employed. For example, consider the following equation for the hue [17]:

$$\theta = \arctan \left(\frac{\sqrt{3}(G - B)}{(R - G) + (R - B)} \right) \quad (23)$$

Equation (21) assigns hue-angle $\theta_h = 0$ to the red channel, hue-angle $\theta_h = 2/3\pi$ to the green channel, and $\theta_h = 4/3\pi$ to the blue channel. Let $\rho_s = 1 - \min\{R, G, B\}$, then the weights of (22) are defined as $w_1 = R - \rho_s$ for the red channel, $w_2 = G - \rho_s$ for the green channel, and $w_3 = B - \rho_s$ for the blue

channel. Substitution of these results into (20) gives

$$\begin{aligned}\theta &= \arctan\left(\frac{(R - \rho_s)\sin(0) + (G - \rho_s)\sin(2/3\pi) + (B - \rho_s)\sin(4/3\pi)}{(R - \rho_s)\cos(0) + (G - \rho_s)\cos(2/3\pi) + (B - \rho_s)\cos(4/3\pi)}\right) \\ &= \arctan\left(\frac{\frac{1}{2}\sqrt{3}G - \frac{1}{2}\sqrt{3}B}{R - \frac{1}{2}G - \frac{1}{2}B}\right) = \arctan\left(\frac{\sqrt{3}(G - B)}{(R - G) + (R - B)}\right)\end{aligned}\quad (24)$$

identical to (23).

The polar coordinates are illustrated in figure (2). The hue polar angle θ_h is invariant to the geometry and specularities: For a multispectral camera with narrow-band filters, consider substitution of (11) in the term $c(\lambda_i) - [1 - \rho_s]$ of (20) as

$$c(\lambda_i) - [1 - \rho_s] = m_b(\vec{n}, \vec{s})[c_b(\lambda_i) - c_b(\lambda_\rho)] \quad (25)$$

where $c_b(\lambda_\rho) = \min\{c(\lambda_1), \dots, c(\lambda_N)\}$. This term is clearly independent of specular term $m_s(\vec{n}, \vec{s}, \vec{v})$. Moreover, the hue polar angle is independent of shadows (i.e. assuming that the light in the shadow has the same spectral characteristics as the light in the non-shadow area) and geometry as the substitution of (25) in (20) gives

$$\theta_h = \arctan\left(\frac{\sum_{i=1}^N [c_b(\lambda_i) - c_b(\lambda_\rho)] \sin[\phi(i, N)]}{\sum_{i=1}^N [c_b(\lambda_i) - c_b(\lambda_\rho)] \cos[\phi(i, N)]}\right) \quad (26)$$

independent of geometric term $m_b(\vec{n}, \vec{s})$. Similar arguments hold for the white-balanced spectral sharpened *RGB*-camera.

The distance between two hue polar angles $\theta_{h,i}, \theta_{h,j}$ is computed as $\Delta(\theta_{h,i}, \theta_{h,j})$ where Δ is defined in (17). Because the hue polar angle is independent of the geometry of the object and independent of shadows and specularities, the distance between two hue polar angles is therefore photometric invariant as well.

3.3 Discussion

The distance between chromaticity angles, $\Delta(\theta_{c,i}, \theta_{c,j})$, is a photometric invariant for shadows (i.e. assuming that a shadow area has the same spectral characteristics as the light source) and the geometry of objects. Similarly, the distance between hue-angles, $\Delta(\theta_{h,i}, \theta_{h,j})$, is a photometric invariant to shadows,

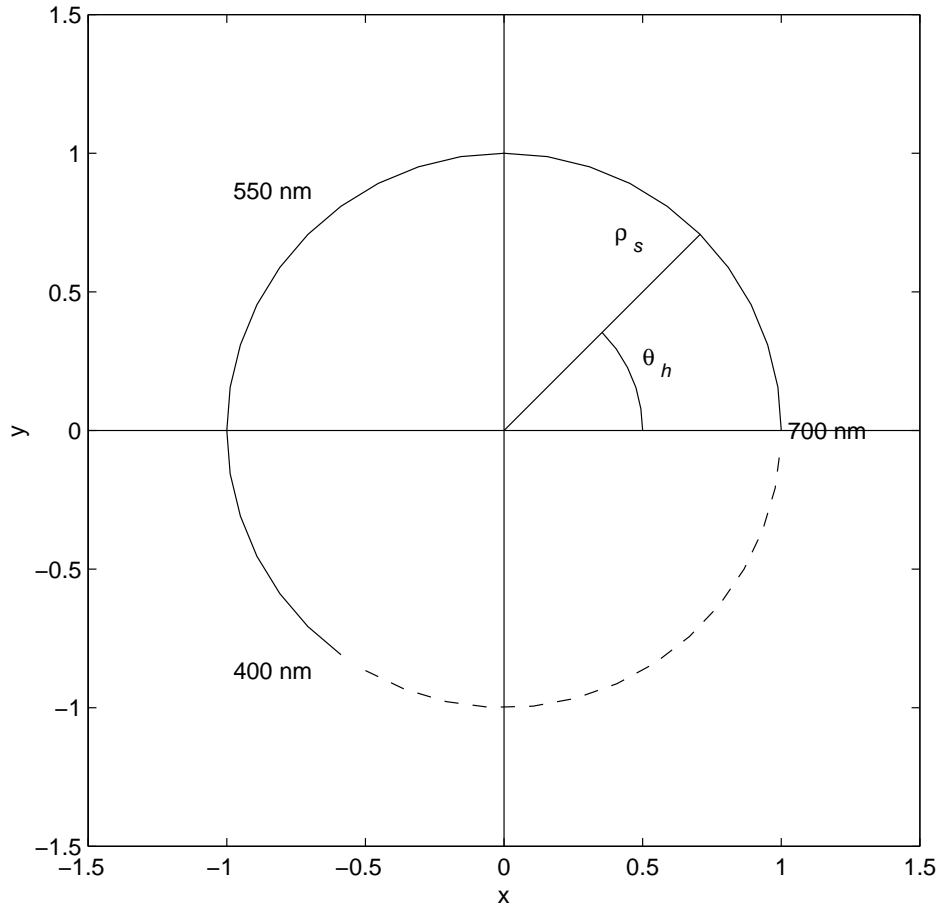


Figure 2: *Polar coordinate representation of a spectrum depicted as a Euclidean map. ρ_s encodes the saturation of the spectrum and θ_h encodes the hue. The hue polar angle forms a unit half plane emanating from the origin in multispectral space. The hue range from $0 \cdots 4/3\pi$ is reserved for the colors ranging from red (700 nm) through green (550 nm) to blue (400 nm). The range from $4/3\pi \cdots 2\pi$ (dashed part of the hue circle) represents purplish colors.*

the geometry and highlights (i.e. again assuming spectrally uniform illumination). These novel invariant measures come at the expense of requiring white balancing.

4 Error Propagation

In general, the result of a measurement of a quantity u is properly stated as

$$\hat{u} = u_e \pm \sigma_u \quad (27)$$

where u_e is the best estimate for the quantity u and σ_u is the uncertainty or error in the measurement of u . Suppose that u, \dots, w are measured with corresponding uncertainties $\sigma_u, \dots, \sigma_w$, and the measured values are used to compute the function $q(u, \dots, w)$. If the uncertainties in u, \dots, w are independent, random and small, then the estimated uncertainty in \hat{q} [23] is

$$\sigma_q = \sqrt{\left(\frac{\partial q}{\partial u} \sigma_u\right)^2 + \dots + \left(\frac{\partial q}{\partial w} \sigma_w\right)^2} \quad (28)$$

The uncertainty in q is never larger than the ordinary sum

$$\sigma_q \leq \left|\frac{\partial q}{\partial u}\right| \sigma_u + \dots + \left|\frac{\partial q}{\partial w}\right| \sigma_w \quad (29)$$

In fact, this equation is really the *upper limit* on the uncertainty as proofed by Taylor [23]. Therefore, whether or not the errors in u, \dots, w are dependent (or normally distributed), the uncertainty in q will never exceed the right side of (29). Therefore, (29) can be used for independent *and* dependent errors and will be used in the following sections to propagate noise through the polar angle representations of spectra.

4.1 Propagation of Uncertainties due to Photon Noise

Modern CCD-cameras are sensitive enough to be able to count individual photons. Photon noise arises from the fundamentally stochastic nature of photon production. The probability distribution for counting ρ photons during t seconds

is known to follow the Poisson distribution. The number of photons measured at pixel x is given by its average as

$$\hat{h}(x) = \rho t \pm \sqrt{\rho t} \quad (30)$$

Let σ_d denote the dark current uncertainty. Incorporating σ_d and the uncertainty of (30) in (1) gives

$$c(x) \pm \sigma_{c(x)} = \gamma[\rho t \pm \sqrt{\rho t}] + [d(x) \pm \sigma_d] \quad (31)$$

Our interest is in computing $\sigma_{c(x)}$. Let the dark current variance be denoted as $\text{var}(d) = \sigma_d^2$. Let the average image intensity measured over a homogeneously colored patch be $\hat{I} = \gamma\rho t$, then the associated variance $\text{var}(\hat{I}) = \gamma^2\rho t$. We have the linear relation between \hat{I} and $\text{var}(\hat{I})$ based on [19] as

$$\text{var}(\hat{I}) + \text{var}(\hat{d}) = \gamma\hat{I} + \text{var}(\hat{d}) \quad (32)$$

Linear regression among some intensity-variance pairs gives a robust estimation of the gain γ . It follows that the uncertainty in the number of photons measured at an arbitrary pixel $c(x)$ is given by

$$\sigma_c^2(x) = [\gamma \cdot c(x)]^2 + \sigma_d^2 \quad (33)$$

4.2 Propagation of Uncertainty

As stated before, in this paper, the Jain CV-M300 camera is used with 576 pixels along the optical axis. We use the Inspector V7 spectrograph, from 410 nm to 700 nm, with wavelength interval of 5 nm. Then the number of spectral samples obtained is 59. In fact, these 59 samples are recorded (uniformly spaced) over the 576 pixels along the optical axis. Therefore, the pixels at position (x, λ) of image h can be averaged in spectral direction by a uniform filter depending on the number of pixels. Let $K' = \text{round}(576/59)$. If K' is odd, then the size of the filter $K = K'$, else $K = K' - 1$. The averaged spectral image h' is

$$h'(x, \lambda) = \frac{1}{K} \sum_{i=y_\lambda - \lfloor K/2 \rfloor}^{y_\lambda + \lfloor K/2 \rfloor} h(x, \lambda_i) \quad (34)$$

The uncertainty in a pixel value is propagated to the uncertainty in polar angles as follows. First, it is assumed that the pixel values in the spectral image are dependent. Therefore, using (29) instead of (28), the uncertainty due to the smoothing operation of (34) reduces to

$$\sigma_{h'}^2(x, \lambda) = \frac{1}{K} \sum_{i=y_\lambda - \lfloor K/2 \rfloor}^{y_\lambda + \lfloor K/2 \rfloor} \sigma_h^2(x, \lambda_i) \quad (35)$$

From (11) it follows that the uncertainty in the white-balanced camera output is

$$\sigma_{c'}^2(x, \lambda_i) = \frac{c^2(x, \lambda_i)\sigma_w^2(x, \lambda_i) + w^2(x, \lambda_i)\sigma_c^2(x, \lambda_i)}{w^4(x, \lambda_i)} \quad (36)$$

where c' denotes the white-balanced camera output and c denotes the observed camera output. w denotes the output for the white matte reference standard.

For the general function $q(u, v) = \arctan(u/v)$ where the parameters u, v are dependent and have associated uncertainties σ_u, σ_v , the uncertainty in output σ_q is obtained using (29) as

$$\sigma_q \leq \left| \frac{v\sigma_u}{u^2 + v^2} \right| + \left| \frac{u\sigma_v}{u^2 + v^2} \right| \quad (37)$$

The function is shown in figure (3). Large uncertainties occur if u and v both approach the value zero. The polar angles of (14) are inter-dependent as each angle is obtained by division through the same value $\theta(\lambda_N)$. The uncertainty in chromaticity polar angle of (14) therefore follows straightforward from (37) by substituting $u = c(\lambda_i)$, $v = c(\lambda_N)$, and where both σ_u and σ_v are obtained from (36).

To obtain an estimate of the uncertainty of the hue polar angle, consider the term $c(\lambda_i) - [1 - \rho_s]$ of (20). The parameters $c(\lambda_i)$ and ρ_s are assumed independent because the reflectance factor $c(\lambda_i)$ is assumed to be obtained independent from the reflectance factor $\rho_s = 1 - \min\{c(\lambda_1), \dots, c(\lambda_N)\}$. Thus, the resulting uncertainty is obtained using (28) as

$$\sigma_{c-[1-\rho]}^2(\lambda_i) = \sigma_c^2(\lambda_i) + \sigma_\rho^2 \quad (38)$$

The uncertainty for the hue polar angle of (20) follows from (22). The exact number generated by (21) has no associated uncertainty, and therefore

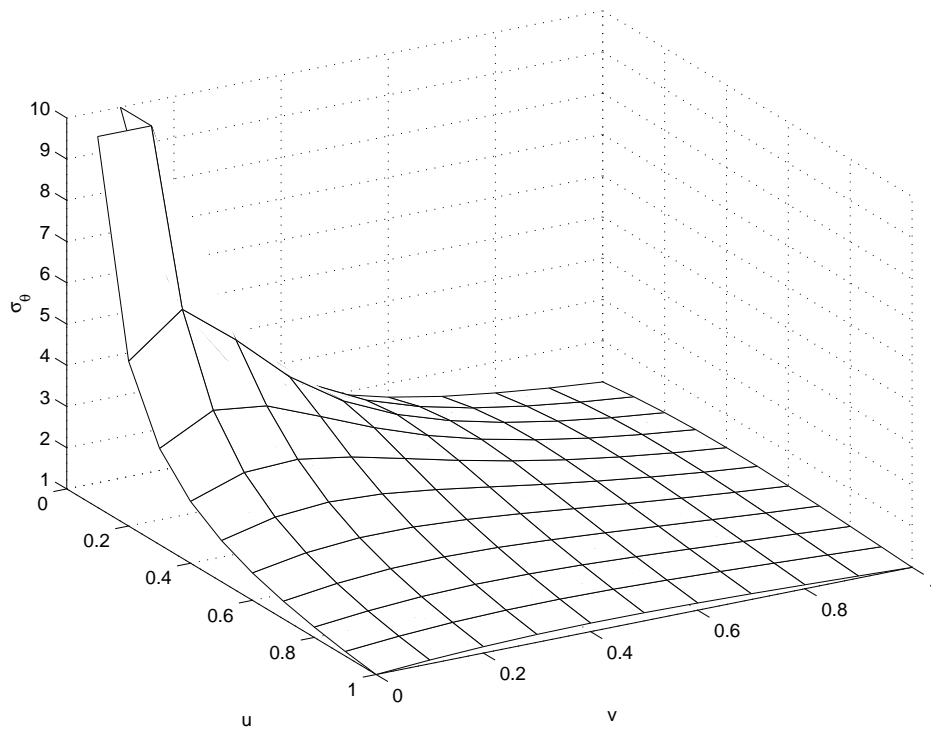


Figure 3: *Uncertainty in the function $\arctan(u/v)$ as function of u and v . The uncertainties σ_u and σ_v are set equal to one. Large uncertainties occur if both u and v approach the value zero, indicating the instability of the function around the origin.*

$\sin[\phi(i, N)]$ has no associated uncertainty. However, the weights $w_i = c(\lambda_i)$ do have uncertainty $\sigma_c(\lambda_i)$, again specified by (36). The individual terms $w_i \sin(\theta_i)$ are considered independent, because the reflectance factor $w_i = c(\lambda_i)$ is assumed to be obtained independent from the reflectance factor at wavelength $w_j = c(\lambda_j)$. Therefore, the uncertainty of the enumerator term $u = \sum_i w_i \sin(\theta_i)$ is

$$\sigma_u^2 = \sum_i (\sigma_c(\lambda_i) \cdot \sin[\phi(i, N)])^2 \quad (39)$$

A similar argument holds for the denominator term $u = \sum_i w_i \cos(\theta_i)$ yielding σ_v . The uncertainty for (22) is then obtained by straightforward substitution of u, σ_u and v, σ_v in (37).

In summary, the uncertainty in the reflectance factors of a spectrum is determined in theory by converting a pixel color value into the number of photons counted at that pixel. Under the assumption that counting photons follows a Poisson distribution, the uncertainty associated with a pixel value is determined. The obtained uncertainty is propagated to the uncertainty in the two polar angle representations of the spectrum.

5 Photometric Invariant Region Detection by Clustering

In section 2, it was shown that uniformly colored objects of matte material draw half-rays in *RGB* and multispectral color space due to changes in the surface orientation, illumination intensity, and shading. In section 3, it was derived that the distance from a spectrum to such half-ray is a photometric invariant. Furthermore, in section (4), we derived for the i -th spectrum $\vec{c}_i, i = 1, \dots, n$ that the uncertainty $\vec{\sigma}_i$ can be obtained using (36). In this section, the uncertainty of the polar angle representations will be incorporated into the image segmentation scheme.

5.1 Robust K -means Clustering

Let a multispectral image consist of spectra \vec{c}_i , $i = 1, \dots, n$, with corresponding uncertainties $\vec{\sigma}_i$. The well-known K -means clustering method [7] segments the image by minimizing the squared error criterion. A clustering is a partition $[\vec{v}_1, \dots, \vec{v}_K]$ that assigns each spectrum to a single partition \vec{v}_j , $1 \leq j \leq K$. The spectra assigned to \vec{v}_j form the j -th cluster. In this paper, we assume that the number K is given.

We compute the cluster center as the weighted average [23]. If M spectra \vec{c}_i with corresponding uncertainties $\vec{\sigma}_i$, $i = 1, \dots, M$, are assigned to a cluster, then the weighted average is computed as

$$\vec{v} = \frac{\sum_{i=1}^M \vec{w}_i \cdot \vec{c}_i}{\sum_{i=1}^M \vec{w}_i} \quad (40)$$

where the weights are the inverse squares of the uncertainties

$$\vec{w}_i = \frac{1}{\vec{\sigma}_i \cdot \vec{\sigma}_i} \quad (41)$$

Since the weight attached to each measurement involves the square of the corresponding uncertainty σ_i , any measurement which is much less precise than the others contributes very much less to the final answer (40). With \vec{c}_i the series of M spectra assigned to the j -th cluster, and with \vec{v}_j the weighted average of the spectra, the squared error for the j -th cluster is:

$$e_j^2 = \sum_{i=1}^M (\vec{c}_i - \vec{v}_j) \cdot (\vec{c}_i - \vec{v}_j) \quad (42)$$

and the squared error for the clustering is:

$$E^2 = \sum_{i=1}^K e_i^2 \quad (43)$$

The objective of the K -means clustering method is to define, for given K , a clustering that minimizes E^2 by moving spectra from one cluster to another.

5.2 Photometric Invariant Segmentation

To obtain photometric invariant region detection, in this paper, we propose to cluster on K straight lines from the origin. Assume that the N -dimensional

spectrum \vec{c} is described by (12) with associated uncertainty $\vec{\sigma}_c$ obtained from (36). The spectrum is transformed to chromaticity polar angles $\vec{\theta}$ by (14) with associated uncertainty $\vec{\sigma}_\theta$ obtained from (37).

To cluster in polar angle space, the angular distance of (16) replaces (42) and the weighted angular average of (22) replaces (40). Given K clusters v , the spectrum is then assigned to the closest cluster. In the next step of the clustering algorithm, new partitions are obtained by moving spectra from one cluster to another. Kender [15] pointed out that color space transforms are unstable for sensor input values near the singularity. As is clear from (37), the instability of the polar angle transformation is the drawback of the polar angle representation of the spectrum. The instability is dealt with by updating the cluster by the weighted sum as defined by (22) where the weights w_j are derived by (41). In other words, transformed polar angles with higher uncertainty contribute much less to the final estimate of the cluster than polar angles with small uncertainty. It was shown that the chromaticity polar angle representation is invariant to changes in the geometry of a uniformly colored object. Therefore, clustering in chromaticity polar angle space yields regions invariant to the geometry. In conclusion, using the uncertainties, we obtain segmentation results invariant to photometric effects and robust against noise.

Similarly, to find homogeneously colored surfaces from glossy materials, we cluster in the hue polar angle representation. For shiny surfaces, the spectrum is transformed to the hue polar angle θ_h by (20) with associated uncertainty σ_{θ_h} obtained from (37). Given K clusters, the distance from the cluster v_j to the spectrum is derived by (16). The spectrum is then assigned to the closest cluster v_i . The instability of the polar angle transformation is again dealt with by updating the cluster using the weighted sum (Equation (22)). In other words, transformed polar angles with higher uncertainty contribute much less to the final estimate of the cluster than polar angles with small uncertainty. In conclusion, it was shown that the hue polar angle representation is invariant to changes in the geometry and specularities. Therefore, clustering in hue polar angle space yields regions invariant to the geometry and specularities. Using the

weighted sum for the updating of cluster centroids achieves robustness against noise.

6 Experiments

All multispectral images are grabbed using a Jain CV-M300 monochrome CCD-camera, Matrox Corona Frame-grabber, Navitar 7000 zoom lens and Inspector V7 spectrograph under 500 Watt halogen illumination. The *RGB* images are grabbed using a Sony 3CCD color camera XC-003P and four Osram 18 Watt “Lumilux deLuxe daylight” fluorescent light sources.

To estimate the values of the electronic gain parameter γ_e (2) and the value of the dark current variance of (32) for the monochrome camera, 19 images are taken of a white reference while varying the lens aperture such that each image has a different intensity as shown in figure (4). A line is fitted through the intensity-variance data yielding an electronic gain of $\gamma = 0.0069$, and dark current variance of $\sigma_d^2 = 0.87$.

The *RGB*-camera has a white-balancing option. The goal is therefore to establish the overall value of the camera gain γ_i where $i \in \{R, G, B\}$. To that end, 26 images are taken of a white reference while repeating the procedure to obtain different intensity images. The data are shown in figure (5). Fitting three lines through a common origin yield a camera gain of $\gamma_R = 0.040$, of $\gamma_G = 0.014$, of $\gamma_B = 0.021$ and dark current variance $\sigma_d^2 = 2.7$.

6.1 Propagation of Uncertainties in Transformed Spectra

Models were proposed in (33, 35, 36) to estimate uncertainties resulting from sensor noise in a spectrum for white-balanced camera systems. The goal of the experiment is to verify empirically the validity of the equations. Therefore, five multispectral images are taken from uniformly colored sheets of paper such that the entire spectral image exhibits one single color. The colors are red, yellow, green, cyan and blue.

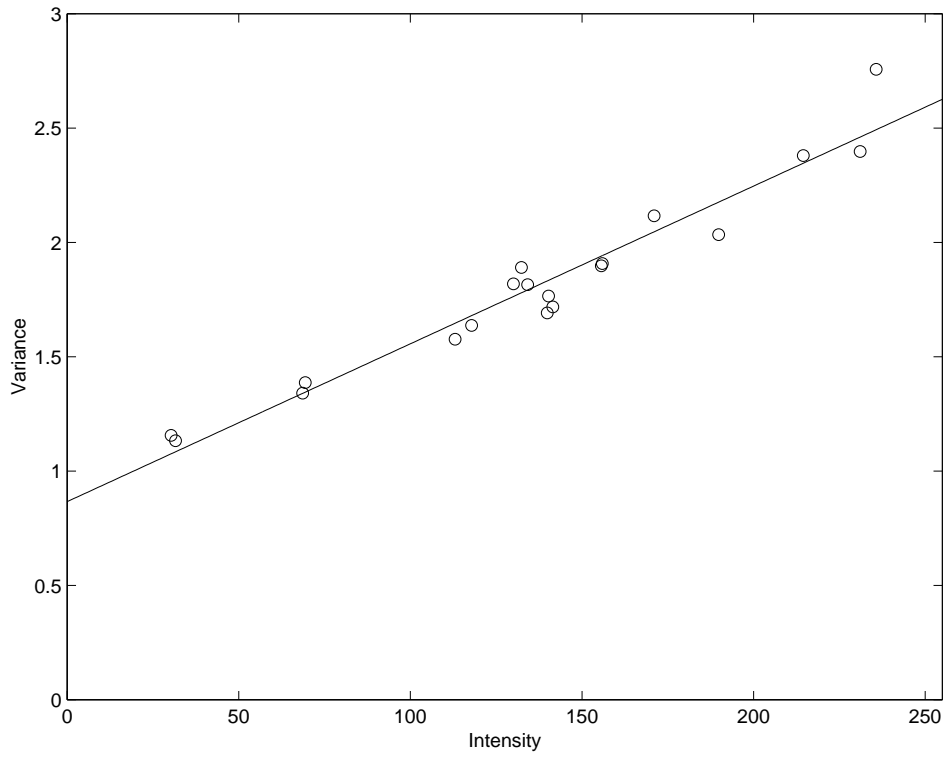


Figure 4: Visualization of the fitted line $var(I) = \gamma I + var(d)$ for the Jain monochrome camera.

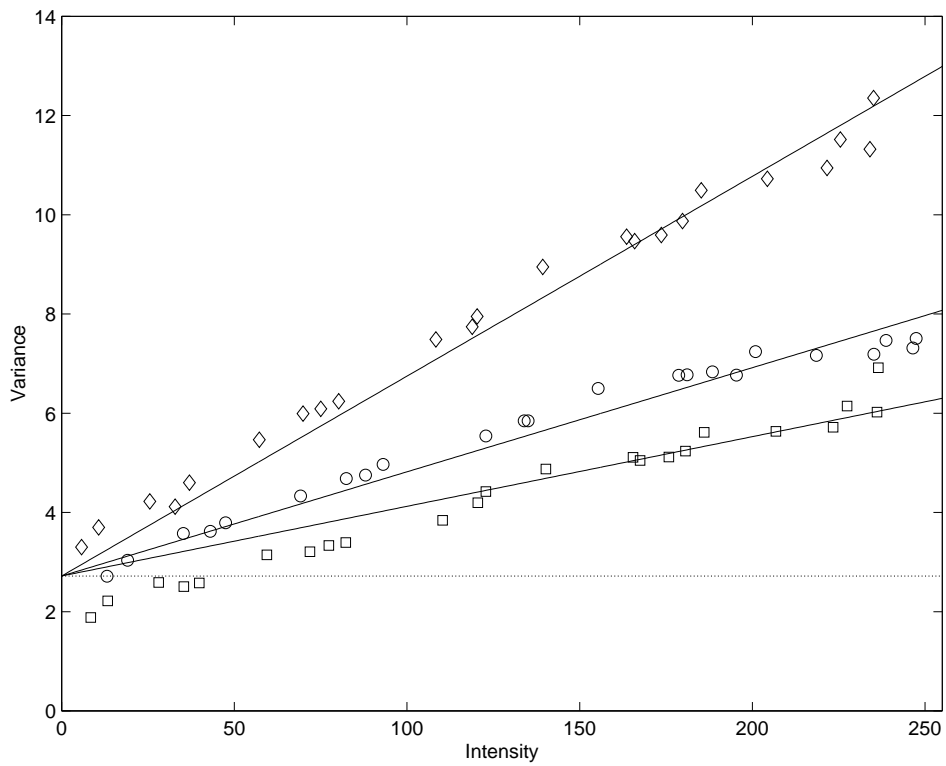


Figure 5: Visualization of the fitted lines $\text{var}(I_i) = \gamma_i I_i + \text{var}(d)$ where $i \in \{R, G, B\}$ for the Sony color camera. Diamonds correspond to the red color channel, squares to green and circles to blue.

Using the gain parameters, the uncertainty in the white-balanced camera output $\hat{\sigma}_c(\lambda)$ can be estimated (33). The estimated uncertainties are averaged for each wavelength over the spatial range as

$$\hat{\sigma}_c(\lambda) = \frac{1}{M} \sum_{i=1}^M \sigma_c(x_i, \lambda) \quad (44)$$

for M pixels along the one-dimensional spatial axis of the multispectral image. The real uncertainty is derived from the standard deviation of reflectance factors $c(\lambda)$ over the spatial range as

$$\sigma^2(\lambda) = \frac{1}{M-1} \sum_{i=1}^M (c(x_i, \lambda) - \bar{c}(\lambda))^2 \quad (45)$$

where $\bar{c}(\lambda)$ denotes the average reflectance factor. The absolute difference $\delta(\hat{\sigma}(\lambda), \sigma(\lambda))$ between the real and estimated error is obtained as

$$\delta(\hat{\sigma}_c(\lambda), \sigma_c(\lambda)) = |\hat{\sigma}_c(\lambda) - \sigma_c(\lambda)| \quad (46)$$

and then averaged over the wavelength range as

$$\delta(\hat{\sigma}, \sigma) = \frac{1}{N} \sum_{i=1}^N \delta(\hat{\sigma}_c(\lambda_i), \sigma_c(\lambda_i)) \quad (47)$$

where N denotes the number of samples taken in the wavelength range. Due to the low sensitivity of the CCD-camera and low transmittance of the illuminant at lower wavelengths, the uncertainty is greater at the lower wavelengths than at higher wavelengths. The reflectance of a spectrum at a certain wavelength is expressed as the reflectance factor $c(\lambda)$ taking on values between 0 and 1. The difference between the estimated and real uncertainty in the reflectance factor is given in table (1) and is approximately 0.01, corresponding to one percent. Therefore, the table shows a very reasonable correspondence between the measured and real uncertainty. This conclusion can be confirmed visually by examination of figure (6).

The estimation of the uncertainty in the chromaticity and hue polar angles by (37) is verified empirically in a similar way. The average of a series of M

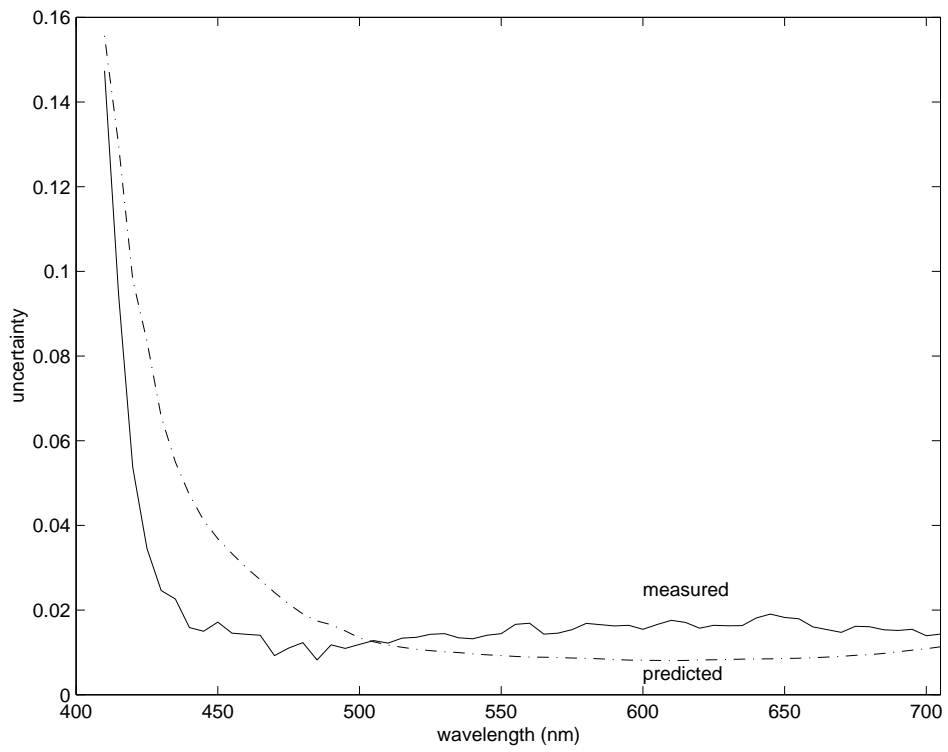


Figure 6: *Yellow paper. Experiment: Comparison of the estimated uncertainty (dashed line) versus the real uncertainty (solid line) of the reflection factors for a yellow paper.*

multispectral	
color	$\delta(\hat{\sigma}(\lambda), \sigma(\lambda))$ (46), Eq. (47)
red	0.011 ± 0.011
yellow	0.011 ± 0.011
green	0.009 ± 0.011
cyan	0.008 ± 0.011
blue	0.006 ± 0.011

Table 1: *Results differentiated for the estimated and real uncertainties in reflectance factors after the white-balancing operation for multispectral images of uniformly colored paper as indicated.*

angular values θ_i , $i = 1, \dots, M$, with equal weights w_i is computed using (22) and is denoted $\bar{\theta}$. The standard deviation is computed as

$$\sigma_{\theta} = \frac{1}{N-1} \sum_{i=1}^N [\Delta(\bar{\theta}, \theta_i)]^2, \quad 0 \leq \bar{\theta}, \theta_i < 2\pi \quad (48)$$

where Δ is defined by (17). Similarly, the difference $\Delta(\hat{\sigma}_{\theta}(\lambda), \sigma_{\theta}(\lambda))$ between the real and estimated error between chromaticity angles at a certain wavelength is obtained using (17). The results are averaged over the wavelength range as

$$\delta(\hat{\sigma}_{\theta}, \sigma_{\theta}) = \frac{1}{N} \sum_{i=1}^N \Delta(\hat{\sigma}_{\theta}(\lambda_i), \sigma_{\theta}(\lambda_i)) \quad (49)$$

The results of the experiment are given in table (2). The dimension of chromaticity polar angles is the number of spectral samples minus one. The second column of the table specifies the results for the spectrograph. The results are averaged over 58 chromaticity angles, therefore the standard deviation is given as well. The third column specifies the results for the *RGB*-camera averaged over 2 chromaticity angles. The chromaticity angles are in the range of zero to 90 degrees, the difference between the estimated and real uncertainty is less than one percent. Consequently, there is a very reasonable correspondence between the measured and real uncertainty. A more detailed example is given in figure (7) for the results for the yellow color.

	multispectral	<i>RGB</i>
color	$\delta(\hat{\sigma}_\theta, \sigma_\theta)$	$\delta(\hat{\sigma}_\theta, \sigma_\theta)$
red	0.6 ± 0.8	1.26
yellow	0.5 ± 0.7	0.01
green	1.6 ± 2.4	0.36
cyan	0.7 ± 0.7	0.11
blue	0.9 ± 1.1	0.07

Table 2: *Results differentiated for the estimated and measured uncertainties in chromaticity polar angles using (49).*

	multispectral	<i>RGB</i>
color	$\delta(\hat{\sigma}_\theta, \sigma_\theta)$	$\delta(\hat{\sigma}_\theta, \sigma_\theta)$
red	0.7	1.1
yellow	0.4	0.5
green	2.1	1.8
cyan	0.5	0.7
blue	1.7	0.5

Table 3: *Results differentiated for the estimated and measured uncertainties in hue polar angles using (17).*

Similarly, for the hue polar angle, the results are given in table (3). The hue angles are in the range of zero to 360 degrees, the difference between the estimated and real uncertainty is less than one percent. Consequently, there is a very reasonable correspondence between the measured and real uncertainty.

6.2 Photometric Invariant Clustering

Multispectral Images Figure (8a) shows a multispectral image of a textile sample. The spectral information is on the vertical axis. The top of the picture corresponds to 410 nm, the bottom to 700 nm. The left-hand side of the

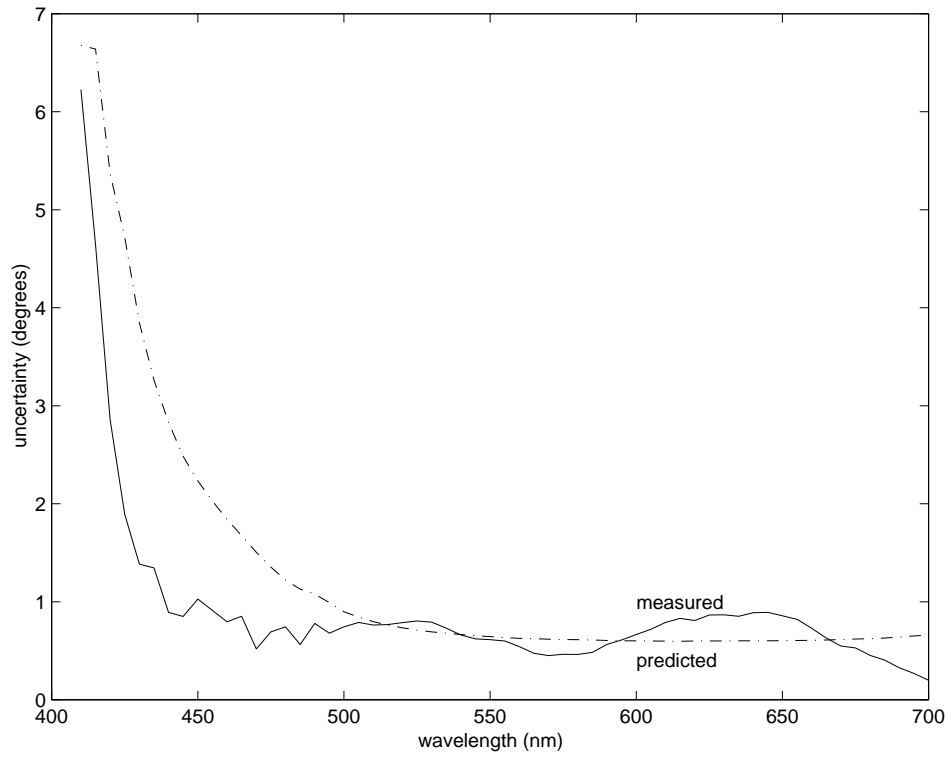


Figure 7: *Yellow paper, uncertainty in chromaticity angle. The absolute difference averaged over the wavelength range is 0.5 ± 0.7 degrees.*

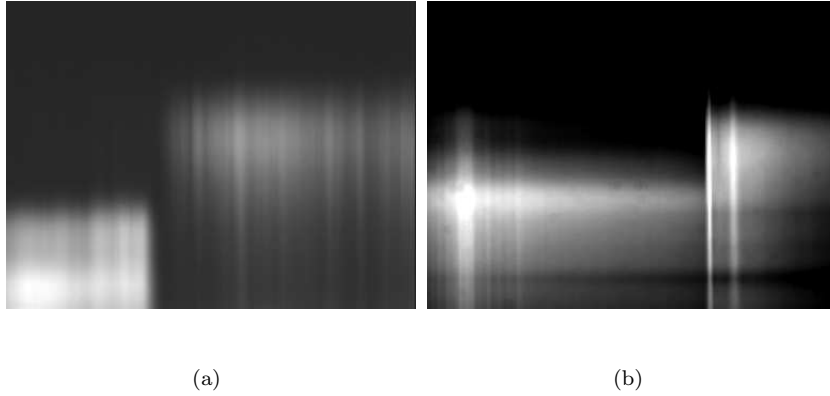


Figure 8: (a) shows a multispectral image of a textile sample. The spatial information is on the horizontal axis, the spectral information is on the vertical axis. The top corresponds to 410 nm wavelength, the bottom to 700 nm wavelength. The left hand side of the image is colored homogeneously red, the right hand side is colored green. The structure of the textile is visible through the intensity fluctuations occurring in the further homogeneous spectra. (b) shows the spectra of two plastic objects. The left hand side object is colored orange, the right hand side object is green. The objects are smooth and structure-less, but reflect specularities showing up as the vertical bright streaks in the spectral image. Furthermore, the intensity of the spectra gradually reduces towards the right hand side of the image due to a change in the surface orientation of the objects.

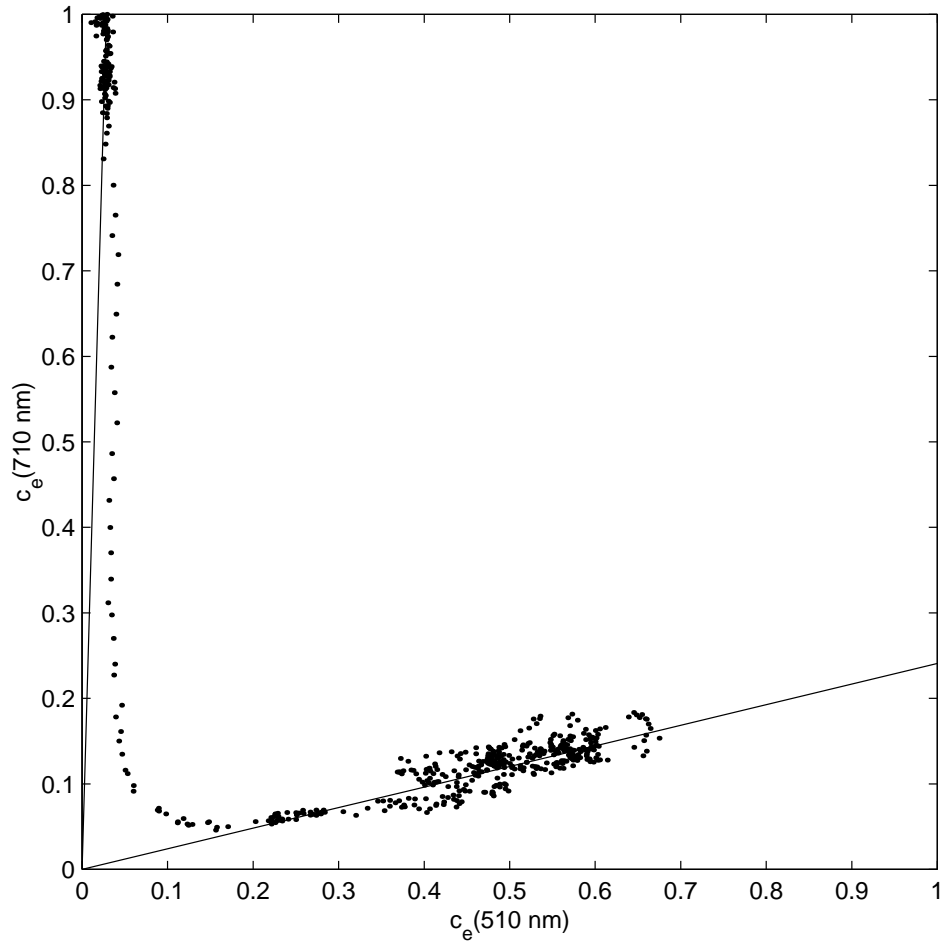


Figure 9: *Result of clustering in the chromaticity polar angle space for the multispectral image shown in figure (8a). The result is shown for the angle between the 510-nm and 710-nm wavelength. The spectra form half-rays due to the geometry changes of the structure of the textile. Fitting of half-rays through the chromaticity angle representation results in invariance for shadows and surface orientation changes.*

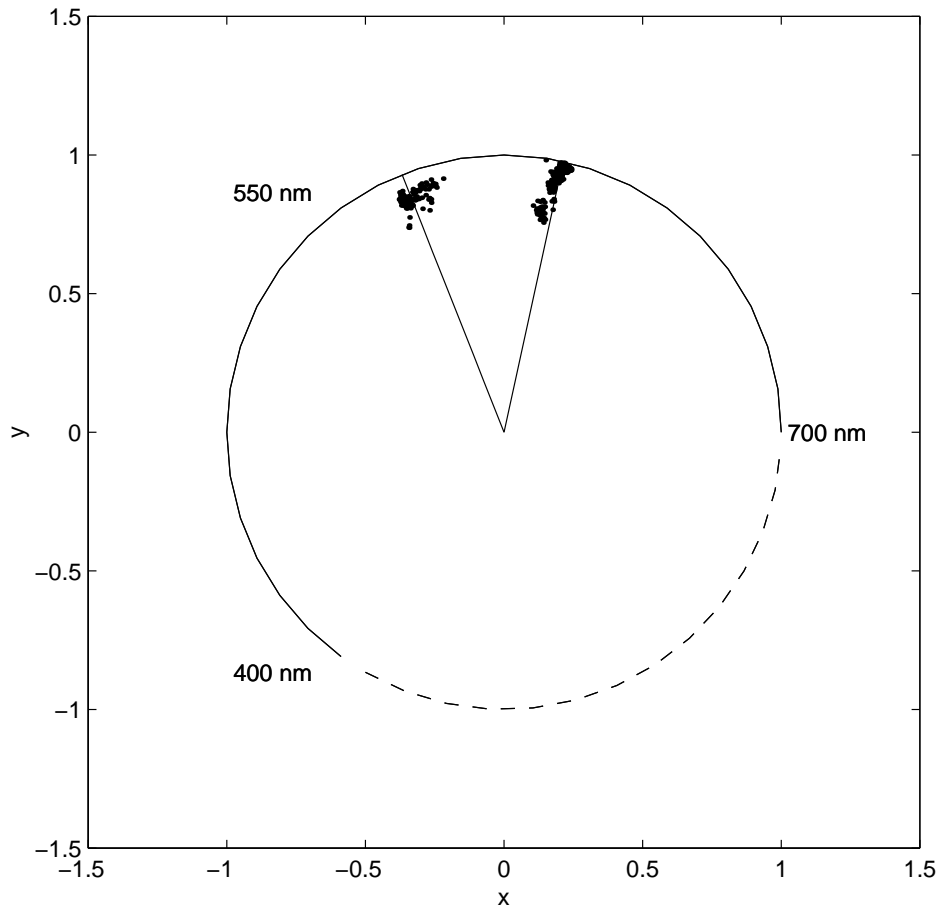


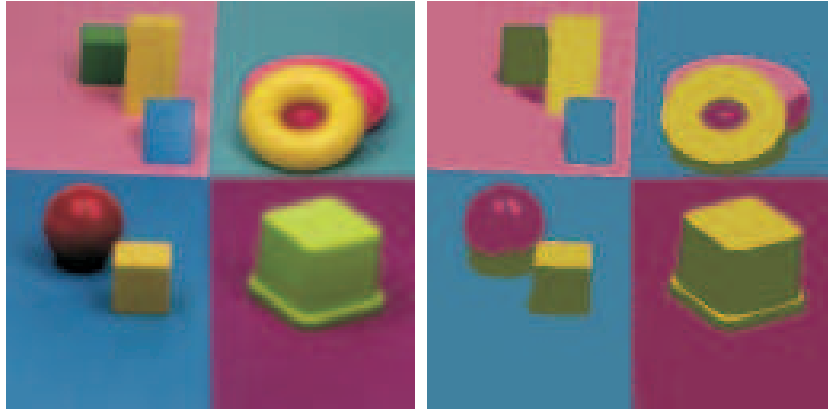
Figure 10: *Result of clustering in hue polar angle space for the image shown in figure (8b). Clustering in hue polar angle representation results in independence to the highlights and surface orientation changes.*

image is from homogeneously red colored textile, the right-hand side is colored green. The structure of the textile is visible in intensity fluctuations occurring in otherwise homogeneous spectra. The result of clustering in the chromaticity polar angle space is shown in figure (9). The figure shows how the spectra form half-rays due to the geometry changes of the structure of the textile. Fitting of half-rays through the chromaticity angle representation results in invariance for shadows and surface orientation changes.

Figure (8b) shows the spectra of two plastic objects. The left-hand side object is colored orange, the right-hand side object is green. The objects are smooth and structure-less, but reflect specularities showing up as the vertical bright streaks in the spectral image. Furthermore, the intensity of the spectra gradually reduces towards the right hand side of the image due to a change in the surface orientation of the objects. The result of clustering in hue polar angle space is shown in figure (10). Clustering in hue polar angle representation results in independence to the highlights and surface orientation changes.

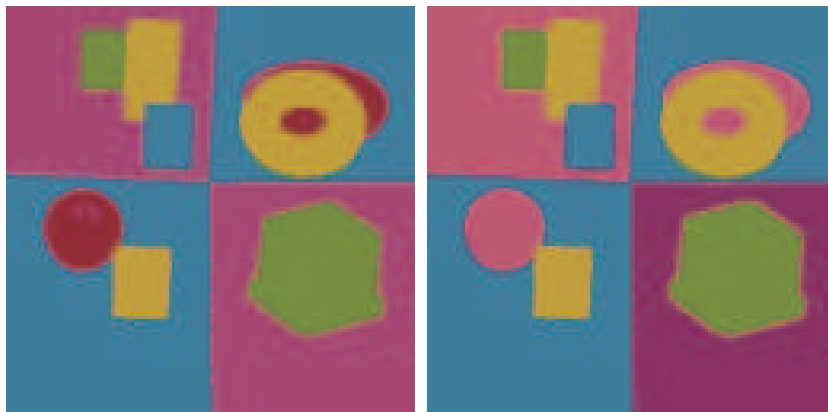
RGB images Figure 11 shows a *RGB*-image of several toys against a background consisting of four squares. The upper-left quadrant of the image consists of three uniformly painted matte cubes of wood. The upper-right quadrant contains two specular plastic donuts on top of each other. In the bottom-left quadrant a red highlighted ball and a matte cube are shown while the last quadrant contains two matte cubes. Each individual object is painted uniformly with a distinct color. The image is contaminated by noise, shadows, shading, and specularities.

In figure (11b) the segmentation result is shown obtained by the *K*-means clustering method in *RGB*-data. False regions are detected due to abrupt surface orientations, shadows, inter-reflections and highlights. In contrast, the result of clustering in the chromaticity polar angle space is shown in figure (11c). Regions are detected insensitive for shadows and surface orientation changes but are affected by highlights. The result of clustering in hue polar angle space is shown in figure (11d). Here, computed region edges correspond to material



(a)

(b)



(c)

(d)

Figure 11: *Segmentation results for the K-means clustering method. a. RGB-image b. Cluster model is a point, region detection is sensitive to intensity changes, shadows, geometry, highlights and color transitions. c. Cluster model is a half-ray, region detection is sensitive to highlights and color transitions. d. Cluster model is a triangularly-shaped plane, region detection is sensitive only to color transitions.*

boundaries discounting the disturbing influences of surface orientation, illumination, shadows and highlights. The difference between figures (11c) and (11d) is the invariance of the latter to the specularities reflected at the red ball.

7 Discussion

We have combined a camera and image formation model to describe how light reflected by an object results in the observed sensor value. Based on the models, we then investigated how uniformly colored objects draw clusters in multispectral color space. We showed that uniformly colored objects of matte materials draw half-rays in multispectral color space due to changes in the surface orientation, illumination intensity and shading. In contrast, due to specularities, shiny objects will draw triangularly-shaped planes in multispectral space. Therefore, we investigated computational models to detect clusters where the cluster shape is modeled as either a half-ray or a triangularly-shaped plane. To that end, different distance measures were proposed. The polar angular representations elegantly allow for photometric invariant detection of both matte and shiny surfaces. However, we also showed that the polar angle representation may become unstable in the presence of sensor noise, a problem shared by other photometric invariant color spaces. To overcome this effect, we examined, in theory and in practice, the propagation of sensor noise to the computation of the polar angles. Taking the simplicity of our camera, noise and error propagation models into account, we showed that a neat correspondence exists between the estimated and real uncertainties. The estimated uncertainty was employed in the region detection method to be robust against sensor noise. Finally, we verified empirically that uniformly colored regions are detected by the proposed clustering method invariant to surface orientation changes, shadows and highlights.

Acknowledgments

The authors are grateful to the anonymous reviewers for their valuable comments.

References

- [1] D. Andoutsos, K. N. Plataniotis, and A. N. Venetsanopoulos. A novel vector-based approach to color image retrieval using a vector angular distance measure. *Computer Vision and Image Understanding*, 75(1/2):46–58, 1999.
- [2] R. Bajcsy, S. W. Lee, and A. Leonardis. Color image segmentation with detection of highlights and local illumination induced by inter-reflections. In *Proceedings of 10th ICPR*, pages 785–790, Atlantic City, NJ, 1990.
- [3] S. Baronti, A. Casini, F. Lotti, and S. Parcinai. Multispectral imaging system for the mapping of pigments in works of art by use of principal-component analysis. *Applied Optics*, 37:1299–1309, 1998.
- [4] P. Bui-Tuong. Illumination for computer generated pictures. *Communications of the Association of Computing Machinery*, 18(6):311–317, 1975.
- [5] P. D. Burns and R. S. Berns. Error propagation analysis in color measurement and imaging. *Color Research Applications*, 22(4):123–129, 1997.
- [6] M. Celenk. A color clustering technique for image segmentation. *Computer Vision, Graphics, and Image Processing*, 52:145–170, 1990.
- [7] R. Dubes and A. K. Jain. Clustering techniques: The user’s dilemma. *Pattern Recognition*, 8:247–260, 1976.
- [8] G. D. Finlayson, M. S. Drew, and B. V. Funt. Spectral sharpening: Sensor transformation for improved color constancy. *Journal of Optical Society of America, A*, 11:1553–1563, 1994.

- [9] Th. Gevers and A. W. M. Smeulders. Color based object recognition. *Pattern Recognition*, 32:453–464, 1999.
- [10] Th. Gevers and A. W. M. Smeulders. Pictoseek: Combining color and shape invariant features for image retrieval. *IEEE Trans. on Image Processing*, 9:102–119, 2000.
- [11] H. Haneishi, T. Hasegawa, N. Tsumura, and Y. Miyake. Design of color filters for recording artworks. In *Proceedings of the IS&T's 50th Annual Conference*, pages 369–372, Springfield, Va., 1997.
- [12] M. Hauta-Kasari, K. Miyazawa, S. Toyooka, and J. Parkkinen. Spectral vision system for measuring color images. *Journal of the Optical Society of America A*, 16(10), 1999.
- [13] G. Healey. Segmenting images using normalized color. *IEEE Transactions on Systems, Man and Cybernetics*, 22(1):64–73, 1992.
- [14] S. Kawata, K. Sasaki, and S. Minami. Component analysis of spatial and spectral patterns in multispectral images. *Journal of the Optical Society of America A*, 4:2101–2106, 1987.
- [15] J. R. Kender. Saturation, hue and normalized color: Calculation, digitation effects, and use. Technical report, Carnegie-Mellon University, November 1976.
- [16] G. J. Klinker, S. A. Shafer, and T. Kanade. A physical approach to color image understanding. *International Journal Computer Vision*, 4:7–38, 1990.
- [17] H. Levkowitz and G. T. Herman. Glhs: A generalized lightness, hue and saturation color model. *Computer Vision, Graphics, and Image Processing: Graphical Models and Image Processing*, 55(4):271–285, 1993.
- [18] J. Liu and Y-H. Yang. Multi-resolution color image segmentation. *IEEE Transactions Pattern Analysis and Machine Intelligence*, 16(7):689–700, 1994.

- [19] J. C. Mullikin, L. J. van Vliet, H. Netten, F. R. Boddeke, G. van der Feltz, and I. T. Young. Methods for ccd camera characterization. In H. C. Titus and A. Waks, editors, *SPIE Image Acquisition and Scientific Imaging Systems*, volume 2173, pages 73–84, 1994.
- [20] Y. Ohta, T. Kanade, and T. Sakai. Color information for region segmentation. *Computer Graphics and Image Processing*, 13:222–241, 1980.
- [21] L. Shafarenko, M. Petrou, and J. Kittler. Histogram-based segmentation in a perceptually uniform color space. *IEEE Transactions on Image Processing*, 7(9):1354–1358, September 1998.
- [22] S. A. Shafer. Using color to separate reflection components. *Color Research Applications*, 10(4):210–218, Winter 1985.
- [23] J. R. Taylor. *An Introduction to Error Analysis*. University Science Books, Mill Valley, CA, 1982.
- [24] S. Tominaga. Multichannel vision system for estimating surface and illumination functions. *Journal of the Optical Society of America A*, 13:2163–2173, 1996.
- [25] S. Tominaga. Spectral imaging by a multichannel camera. *Journal of Electronic Imaging*, 8(4):332–341, October 1999.
- [26] L. Wolff, S. A. Shafer, and G. E. Healey, editors. *Physics-based vision: principles and practice*, volume 2. Jones and Bartlett, Boston etc., 1992.